Supporting information

The controllable loading of Fe/Co alloy on heteroatom doped hollow graphene spheres realized by small molecule regulation for rechargeable zinc-air batteries

Yefei Ma[a,b,+], Qiushi Wang [a,+], Xia Xiao [a], Zhong-Jie Jiang [c,*], Weiheng Chen [d], Xiaoning Tian[b,*], Zhongqing Jiang [a,*]

[a] Department of Physics, Zhejiang Sci-Tech University, Hangzhou 310018, P. R. China. Email address: zhongqingjiang@zstu.edu.cn.

[b] Department of Materials and Chemical Engineering, Ningbo University of Technology, Ningbo 315211, P.R. China.

[c] Guangdong Engineering and Technology Research Center for Surface Chemistry of Energy Materials & Guangzhou Key Laboratory for Surface Chemistry of Energy Materials, New Energy Research Institute, College of Environment and Energy, South China University of Technology, Guangzhou 510006, P. R. China. Email address: eszjiang@scut.edu.cn.

[d] Department of Mechanical Engineering, Ningbo University of Technology, Ningbo 315336, P. R. China.

[+] These authors contributed equally.

1. Experimental section

1.1. Reagents and materials

Flake graphite (325 meshes) was bought from Alfa Aesar. Concentrated sulfuric acid (H_2SO_4, 96.0%), sodium nitrate ($NaNO_3$, ≥ 99.0%), hydrochloric acid (HCl, 37.0%), potassium hydroxide (KOH, ≥85.0%), potassium permanganate ($KMnO_4$, ≥ 99.5%), hydrogen peroxide aqueous solution (H_2O_2, 30.0%), 2, 2'-Azobis(2-methylpropionamidine) dihydrochloride (97.0%), polyvinyl pyrrolidone (K-30), styrene (C_8H_8, ≥ 99.5%), melamine ($C_3H_6N_6$, ≥ 99.0%), trisodium citrate ($Na_3C_6H_5O_7·2H_2O$, ≥ 99.0%), Cobalt(II) acetate tetrahydrate ($C_4H_6CoO_4·4H_2O$, ≥ 99.5%), potassium ferricyanide ($K_3FeC_6N_6$, ≥ 99.5%), zinc acetate ($Zn(Ac)_2$, ≥ 99.0%), polyvinyl alcohol (PVA, 99.0%), and isopropanol ($CH_3CH(OH)CH_3$, ≥ 99.7%) were bought from Shanghai Chemical Reagent Co. Ltd. Carbon paper (CP), Carbon cloth, commercial 20% Pt/C were purchased from Shanghai Hesen Electric Co., Ltd. (Shanghai, China). RuO_2 (99.9%) and Zinc foil (99.994%) was purchased from Alfa Aesar. Nafion (5.0 wt.%) was purchased from DuPont Company. All the chemicals were used as received without further purification.

1.2. Material synthesis

1.2.1 Preparation of polystyrene spheres (PS)

The positively charged polystyrene spheres (PS) were prepared by the emulsifier-free polymerization method described previously.[1] 13.0 mL styrene monomer and 1.5 g polyvinyl pyrrolidone (PVP) were dissolved in 100 mL of deionized (DI) water. The mixture was stirred for 30 min at room temperature under the protection of nitrogen. Then, 0.26 g 2, 2'-Azobis(2-methylpropionamidine) dihydrochloride (AIBA) solution was added to the above-mentioned mixture under stirring and the protection of nitrogen for 1 h, which was dissolved in 20 mL DI water. Then, the reaction temperature was raised to 70 ℃, and the reaction was kept under N_2 protection condition for 24 h.

1.2.2 Preparation of FeCo@NGHS, Fe@NGHS, Co@NGHS, Fe&Co@NGHS, FeCo@GHS and NGHS

First, 1 g of PS was dispersed in 25 mL of sodium citrate aqueous solution

containing 1 g of sodium citrate. Then, 50 mg of graphene oxide (GO) was added to the mixture and stirred vigorously for 12 h (The preparation of GO follows the previous method.[1]). After that, 2 g of melamine was added, and the stirring was continued for 11 h. 20 mL of cobalt acetate aqueous solution was slowly added to the mixture and maintained at room temperature for 1 h. After 1 h of stirring and dispersion, 20 mL of potassium ferricyanide aqueous solution was added dropwise to the mixture and stirred for 24 h. The filter cake was collected by suction filtration under reduced pressure, and washed twice with a small amount of DI water. The obtained filter cake was dried at 60 °C overnight, calcined at 420 °C for 3 h under N_2 atmosphere, then further heated to 900 °C at 5 °C min^{-1}, held for another 1 h, and then cooled to room temperature to obtain FeCo@NGHS.

As a comparison, Fe@NGHS and Co@NGHS were further synthesized, but the metal precursors were replaced with potassium ferricyanide or cobalt acetate, respectively, in the same procedure. In addition, nitrogen-doped graphene hollow spheres (NGHS) were also prepared without adding potassium ferricyanide and cobalt acetate but keeping other experimental parameters unchanged. In order to compare and verify the effect of buffer sodium citrate and melamine, the control samples Fe&Co@NGHS and FeCo@GHS were prepared by the same procedure without sodium citrate and melamine, respectively.

1.3. Materials characterizations

The morphologies of obtained samples were characterized using field-emission scanning electron microscopy (S-4800, Hitachi) with an operation voltage of 20.0 kV. Transmission electron microscopy (TEM) and high-resolution TEM (HRTEM) were performed on JEM 2010, JEOL, Japan at an accelerate voltage of 200 kV. The structure analysis was carried out by Bruker D8 Advance X-ray powder diffractometer using Cu Kα radiation (λ = 1.5406 nm) from 5 ° to 85 ° at a scan rate of 2 ° min^{-1}, which operated at voltage 40 kV, current 30 mA. The Brunauer-Emmett-Teller (BET) specific surface area and porosity of obtained samples were detected by Quantachrome, Autosorb-IQ-MP instrument. The composition and chemical states were determined by X-ray

photoelectron spectroscopy (XPS) on Thermo VG Scientific ESCALAB 250 spectrometers with Al Kα radiation source (1486 eV). The thermogravimetric analysis (TGA) (Netzsch, TG209 F3) was operated in air at a heating rate of 5 °C min^{-1} from 30 °C to 800 °C.

1.4. Electrochemical measurements

All the electrochemical measurements tests were conducted at 25 ℃ using CHI 760E electrochemical workstation (Shanghai Chenhua Co., China). The conventional three-electrode system was employed, including the polished glassy carbon rotating disk electrode (GC, 0.19625 cm^2) loaded with the required catalysts as the working electrode, the saturated calomel electrode (SCE) as the reference electrode, and a Pt wire as the auxiliary electrode, respectively. The electrocatalyst inks were prepared by ultrasonically dispersing 4 mg acquired sample in a mixture solution containing 652 μL DI water, 87 μL 5 wt% Nafion, and 261 μL isopropanol. 10 μL dispersed ink was coated onto the GC electrode with a mass loading ~ 0.2 mg cm^{-2} for catalyst, then dried in air. All measured potentials were reported versus the standard reversible hydrogen electrode (RHE), and for conversion of the tested potential (vs. Hg/Hg_2Cl_2) is according to the following formula:

$$\mathrm{E(RHE)} = \mathrm{E(SCE)} + 0.059pH + 0.2415 \quad \text{(S1)}$$

All the OER tests were subsequently tested in 0.1 M KOH solution. The OER linear polarization curves (LSVs) were recorded at scan rate 5 mV s^{-1} ranged between approximately 1.1 and 1.9 V and the data were 80% IR compensated. According to the polarization curves, the Tafel slopes were calculated using the Tafel equation as follows:

$$\eta = a + b \log (j) \quad \text{(S2)}$$

where η, a, b and j are the overpotential, Tafel constant, Tafel slope and measured current density, respectively. The overpotential (η) were measured as follows: η (V) = E (vs. RHE)-1.23 V. The electrochemical impedance spectroscopy (EIS) measurements were conducted at 0.621 V (vs. SCE) in the frequency range of 0.01-100000 Hz. Furthermore, the OER durability was evaluated by chronopotentiometric measurements at 10 mA cm^{-2} with 0.1 M KOH electrolyte. Commercial RuO_2 catalyst were also

measured for comparison.

All the measurements were carried out in 0.1 M KOH solution for ORR performances. The Tafel slopes calculation is the same as OER. The 0.1 M KOH was bubbled with N_2 or O_2 for at least an hour before cyclic voltammetry (CV) tests, and CV curves were tested at a scan rate of 10 mV s^{-1}. The electrochemical impedance spectroscopy (EIS) was measured at -0.156 V (vs. SCE) with the frequency range from 100000 Hz to 0.01 Hz.

The LSVs were performed at various rotation speeds (i.e., 400, 625, 900, 1225, 1600 and 2025 rpm) due to the diffusion-controlled oxygen reduction reaction (ORR). The kinetic current density and the number of electrons transferred (n) could be calculated from Koutecky-Levich (K-L) plots as the following equation:[2]

$$\frac{1}{J} = \frac{1}{J_L} + \frac{1}{J_K} = \frac{1}{(B\omega^{1/2})} + \frac{1}{J_K} \quad \text{(S3)}$$

$$\mathrm{B} = 0.62\mathrm{nF}C_0{D_0}^{2/3}\nu^{-1/6} \quad \text{(S4)}$$

$$J_K = nFkC_0 \quad \text{(S5)}$$

where J, J_k and J_L are the measuring current density, kinetic current density and diffusion limited current density, respectively, while other parameters explain as follows: the reciprocal slope (B), the angular velocity of electrode rotation (ω), the electron transferred number (n), the Faraday constant (96485 C mol^{-1}), the saturated concentration of O_2 in 0.1 M KOH (1.2×10^{-3} mol L^{-1}), the diffusion coefficient of O_2 in 0.1 M KOH (1.90×10^{-5} cm^2 s^{-1}), the kinetic viscosity of 0.1 M KOH (0.01 cm^2 s^{-1}), and the electron transfer rate constant (k).

RRDE voltammetry were performed at 1600 rpm with a scan speed of 5 mV s^{-1}, and the potential of Pt ring electrode was held at 1.3 V (vs. RHE). The electron transfer number (n) and the hydrogen peroxide yield (H_2O_2%) per oxygen molecule can be calculated by the following equations:

$$\mathrm{n} = \frac{4I_D}{I_D + {I_R}/{N}} \quad \text{(S6)}$$

$$H_2O_2\% = 200\frac{{I_R}/{N}}{I_D + {I_R}/{N}} \quad \text{(S7)}$$

where I_D, I_R and N stand for the disk current, the ring current and ring collection

efficiency of RRDE, respectively. In this measurement, N=0.4.

For the Tafel plot, the kinetic current density measured at a rate of 5 mV s^{-1} with a rotating speed from 1600 rpm was calculated from the mass-transport correction of the RDE data by:

$$J_K = \frac{J \times J_L}{(J_L - J)} \quad \text{(S8)}$$

The corresponding bifunctional activity parameter was evaluated by ΔE using the following equation:

$$\Delta E = E_{OER,j=10} - E_{1/2} \quad \text{(S9)}$$

where $E_{OER,j=10}$ and $E_{1/2}$ are the potential at 10 mA cm^{-2} for OER and half of J_L for ORR, respectively.

The ORR stabilities were examined by chronoamperometry method at constant potential of -0.156 V (vs. SCE) for 10000 s. Furthermore, the poisoning durabilities were performed by the addition of CO and methanol. For comparison, the commercial 20% Pt/C catalysts were operated with the same procedure.

1.5. Fabrication of rechargeable ZAB and all-solid-state ZAB

The performance of home-made liquid Zn-air battery (ZAB) were accessed using electrochemical working station (Princeton Applied Research, P2000, USA) under ambient conditions. The as-prepared FeCo@NGHS catalysts, and the commercial physically mixed catalysts of 20% Pt/C and RuO_2 (denoted as 20% Pt/C + RuO_2, mass ratio of 1:1) casted onto gas diffusion layer based carbon paper with catalyst loading of 1 mg cm^{-2} fabricated as the air electrode. A polished Zn plate and a 6 M KOH solution mixed with 0.2 M $Zn(Ac)_2$ were used as the anode and electrolyte, respectively.

Firstly, for the assembling and evaluation of all-solid-state ZAB, the air cathode was fabricated by dropping the FeCo@NGHS ink onto the carbon cloth with catalyst loading of 1.0 mg m^{-2}. The polished zinc sheet was used as anode. The gel polymer electrolyte was prepared as follows: 1 g polyvinyl alcohol powder (PVA) was dissolved in 10 mL DI water and stirred 30 minute at ~ 95 ℃, then 1 mL of 18 M KOH solution with 0.2 M $Zn(Ac)_2$ was added and stirred at ~95 ℃ for ~1 h. Subsequently, the obtained homogeneous solution was transferred to atmosphere of -10 ℃, and then

thawed at room temperature environment to obtain the gelatin for further use. Finally, the flexible all-solid-state ZAB was assembled by placing the air electrode and polished Zn sheet on the two sides of PVA gel.

2. Supplementary Figures and Tables

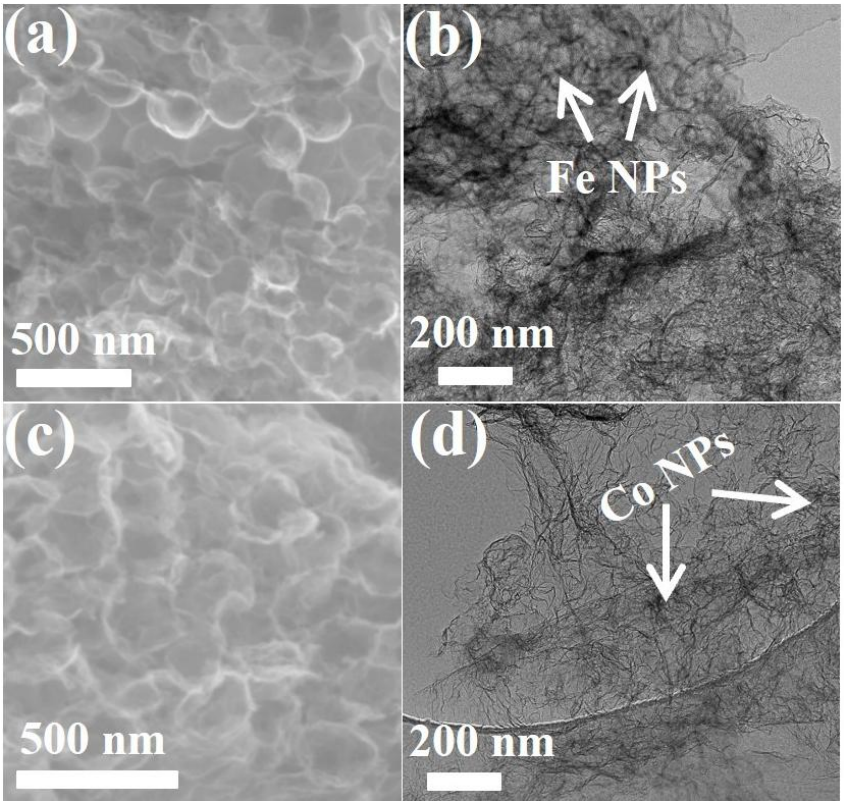

Figure S1. SEM and TEM images of (a, b) Fe@NGHS, and (c, d) Co@NGHS.

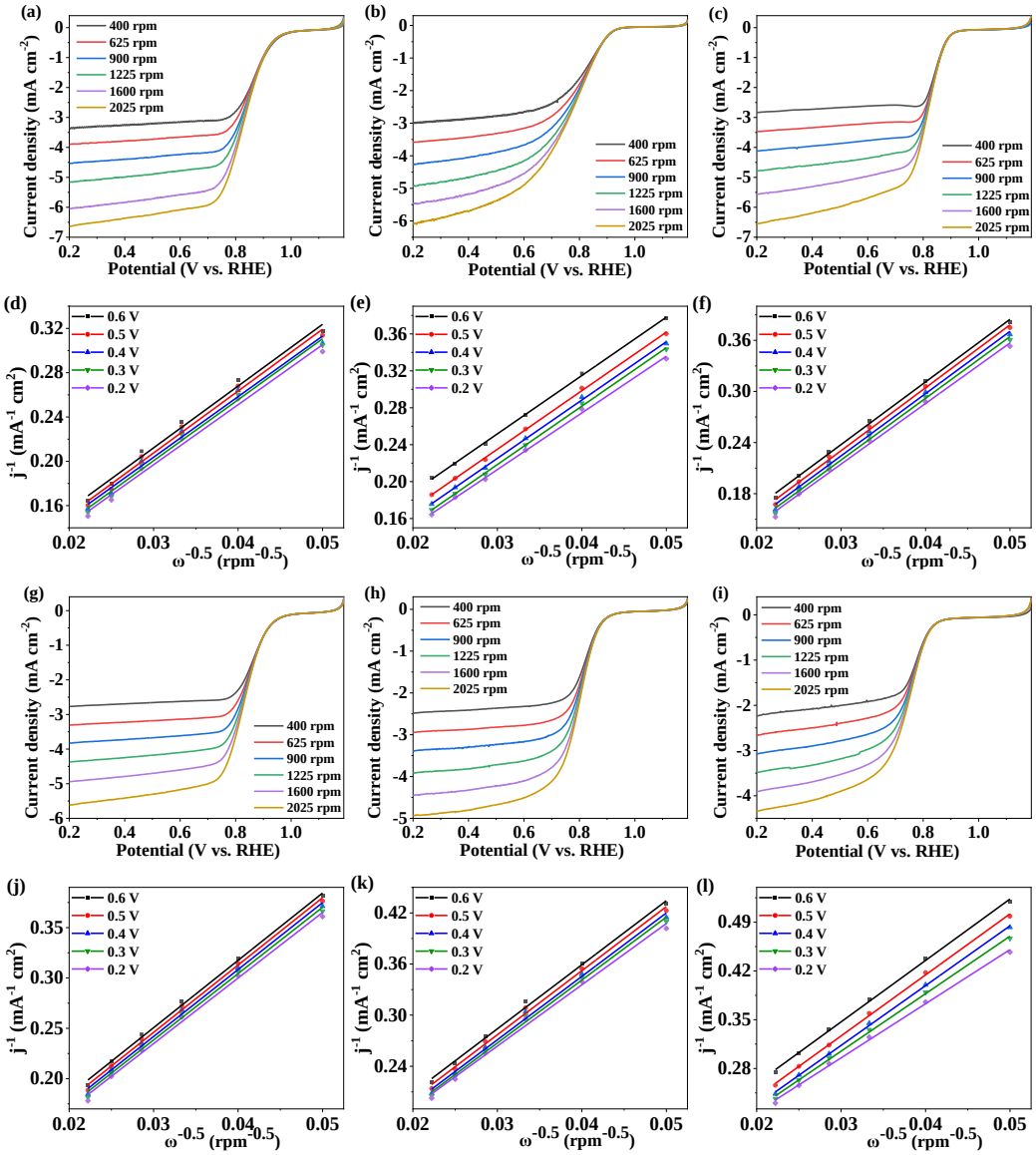

Figure S2. LSV curves measured at different rotation rates on the rotating disk electrode (scan rate: 5 mV s^{-1}) of FeCo@NGHS (a), Fe@NGHS (b), Co@NGHS (c), Fe&Co@NGHS (g), FeCo@GHS (h) and NGHS (i) in O_2-saturated 0.1 M KOH; Based on the LSV data in (a, b, c, g, h, i), the Koutecky-Levich curves of each catalyst were obtained: FeCo@NGHS (d), Fe@NGHS (e), Co@NGHS (f), Fe&Co@NGHS (j), FeCo@GHS (k) and NGHS (l).

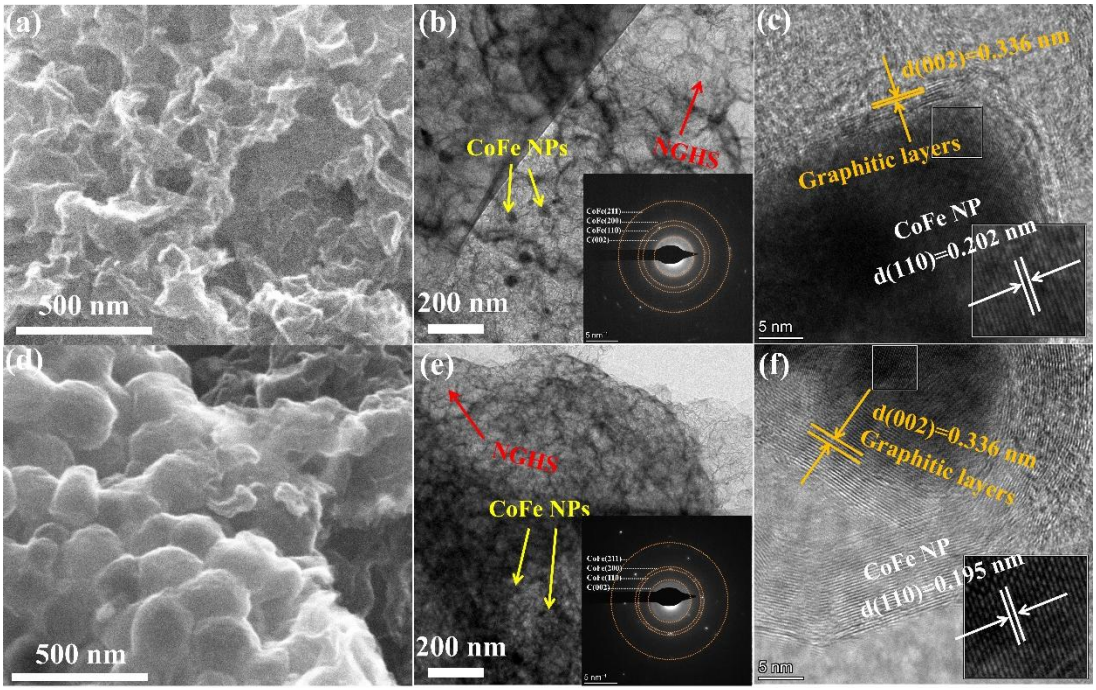

Figure S3. SEM, TEM and HRTEM images of FeCo@NGHS after (a, b, c) ORR stability test and (d, e, f) OER stability test. The insets of (b) and (e) are SAED patterns.

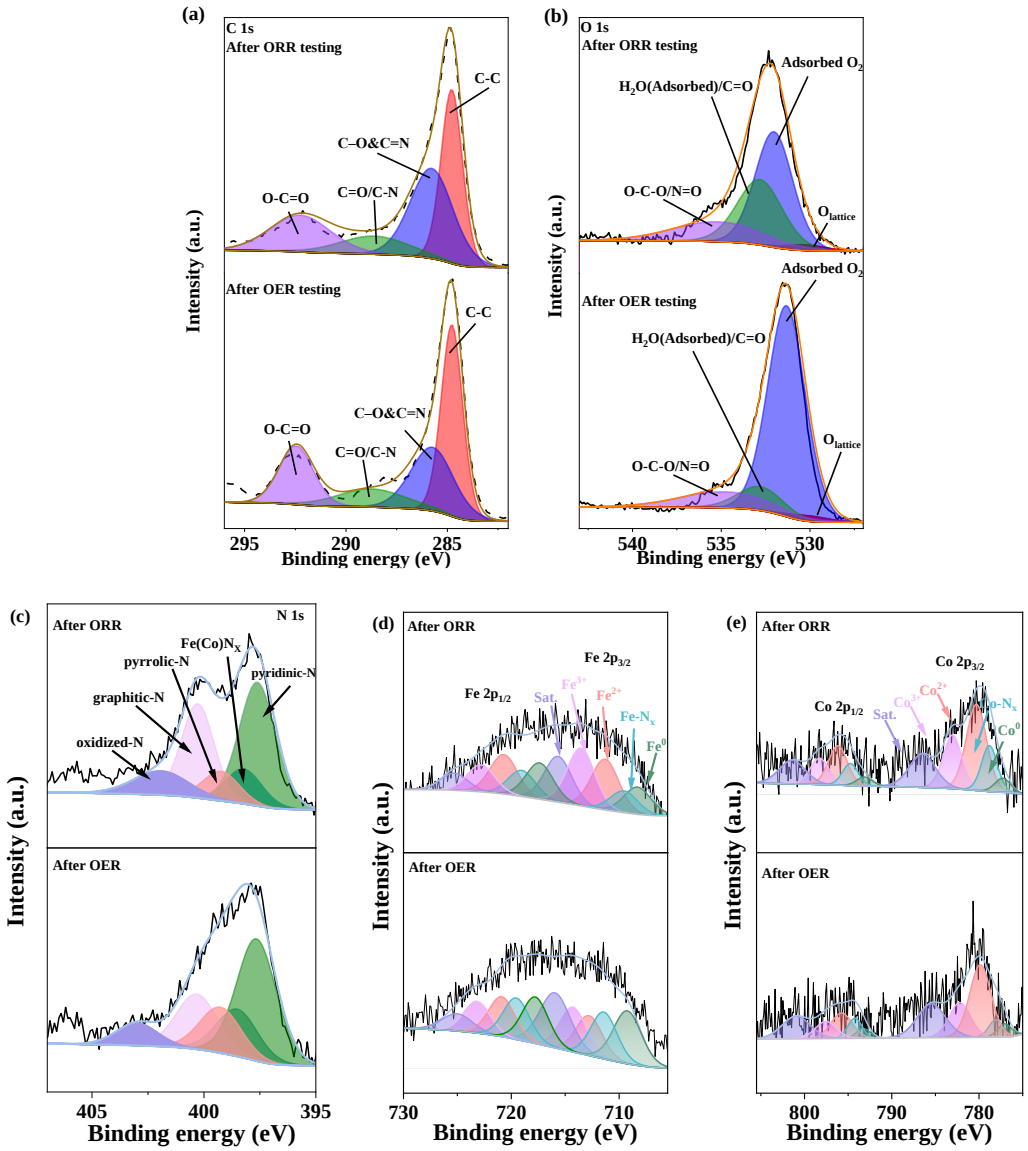

Figure S4. High-resolution XPS spectra of (a) C 1s, (b) O 1s, (c) N 1s, (d) Fe 2p and (e) Co 2p of FeCo@NGHS after ORR and OER stability tests.

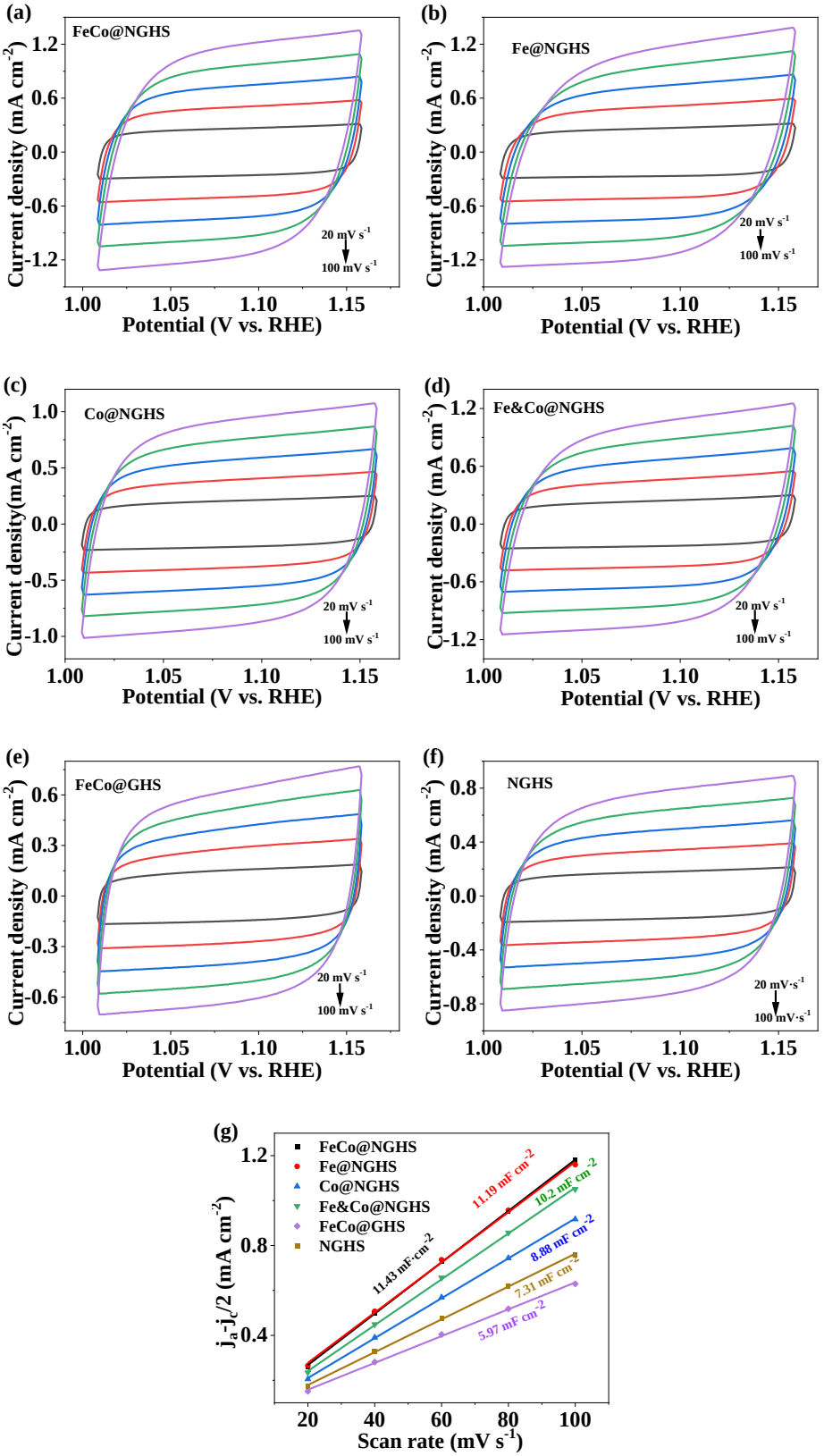

Figure S5. Measured CV curve of (a) FeCo@NGHS, (b) Fe@NGHS, (c) Co@NGHS, (d) Fe&Co@NGHS, (e) FeCo@GHS, (f) NGHS in O_2-saturated 0.1 M KOH at different scan rates; (g) ECSA.

Table S1. The content of metal elements in the catalysts obtained by Inductively coupled plasma mass spectrometry (ICP-MS) testing.

Catalyst	Elemental content (wt.%)	
	Co	Fe
FeCo@NGHS	2.62	2.06
Fe@NGHS	-	0.82
Co@NGHS	0.87	-
Fe&Co@NGHS	4.75	2.55
FeCo@GHS	2.15	1.48

Table S2. The ratio of each nitrogen component is determined by peak fitting of high-resolution N1s XPS spectrum.

Catalyst	Pyridinic-N		$Fe(Co)N_x$		Pyrrolic-N		Graphitic-N		Oxidized-N	
	Binding energy (eV)	Content (%)	Binding energy (eV)	Content (%)	Binding energy (eV)	Content (%)	Binding energy (eV)	Content (%)	Binding energy (eV)	Content (%)
FeCo@NGHS	398.45	42.5	399.38	8.5	400.14	5.1	400.98	28.2	402.98	15.8
Fe@NGHS	398.25	51.9	399.30	6.9	400.14	7.9	400.98	20.8	402.98	12.6
Co@NGHS	398.25	44.6	399.38	4.8	400.14	3.9	400.84	29.5	402.98	17.2
Fe&Co@NGHS	398.45	37.5	399.38	6.1	400.14	4.1	400.98	30.4	402.98	22.0

FeCo@GHS	398.45	31.1	-	-	400.14	7.2	401.00	32.0	402.78	29.7
NGHS	398.11	52.1	-	-	400.14	16.9	401.00	18.5	403.00	12.5

Table S3. The content of each oxygen species is determined by peak fitting of high-resolution O1s XPS spectrum.

Sample	$O_{lattice}$		Adsorbed O_2		H_2O(Adsorbed)/C=O		O-C-O/N-O	
	Binding energy (eV)	Content (%)	Binding energy (eV)	Content (%)	Binding energy (eV)	Content (%)	Binding energy (eV)	Content (%)
FeCo@NGHS	530.06	3.46	531.42	50.57	532.80	24.37	534.66	21.59
Fe@NGHS	529.80	1.85	531.26	31.73	532.74	25.08	534.35	41.32
Co@NGHS	530.08	6.75	531.64	44.63	533.05	21.11	534.88	27.49
Fe&Co@NGHS	530.11	8.47	531.44	49.59	532.88	18.56	534.72	23.36
FeCo@GHS	530.20	9.04	531.49	32.33	533.09	32.28	534.98	26.34

Table S4. Electrocatalytic properties of FeCo@NGHS and recently reported transition metal-based carbonaceous catalysts for ORR and OER.

Catalysts	ORR		OER	ΔE (V vs. RHE)	Reference
	E_{onset} (V vs. RHE)	$E_{1/2}$ (V vs. RHE)	$E_{j=10}$ (V vs. RHE)		
$NiFe_3$@NGHS-NCNTs	0.961	0.846	1.621	0.775	This work
$FeNi_3N$/NG	0.88	0.79	1.64	0.85	[3]
Ni_3Fe/N-C sheets	0.90	0.78	1.6	0.82	[4]
Ni_3FeN/NRGO	1.38	0.75	1.63	0.88	[5]
Ni_3FeN microspheres	-	0.78	1.585	0.805	[6]
FeNi-NC	0.98	0.83	1.61	0.78	[7]
NiFe-ND/FeCo-NC	0.93	0.85	1.66	0.81	[8]
$FeCo_2O_4$/hollow graphene (HG)	0.92	0.82	1.65	0.83	[9]
$CoFe_2O_4$/CNTs	0.904	0.75	1.65	0.9	[10]
CoFe/N-C	1.03	0.821	1.665	0.844	[11]
CoFe@NCNTs	0.95	0.84	1.68	0.84	[12]
NiCo/PFC	0.86	0.79	1.63	0.84	[13]
$NiCo_2O_4$	0.93	0.78	1.62	0.84	[14]
NC-$FeCoNiMn_4$	0.94	0.86	1.6	0.74	[15]
Co/N-Pg	0.81	0.82	1.63	0.81	[16]
NPCGFs	0.86	0.79	1.69	0.9	[17]
Co/N/S-CF	0.92	0.814	1.61	0.796	[18]
3d-GMC	0.947	1.02	1.65	0.63	[19]
CoFeP@NBC	-	0.82	1.47	0.65	[20]
MC@NC	0.99	0.82	1.6	0.78	[21]
C@Co(OH)Se	0.90	0.79	1.57	0.78	[22]

Co_3S_4@Co_3O_4/NSC	-	0.822	1.542	0.72	[23]
BNPC	0.894	0.793	1.38	0.587	[24]

Table S5. Summary of impedance fitting data for catalysts during ORR.

Catalyst	Impedance (Ω)			CPE1(mF)		CPE2(mF)	
	R_s	R_{int}	R_{ct}	CPE1-T	CPE1-P	CPE2-T	CPE2-P
FeCo@NGHS	48.22	52.06	39.96	2.23×10^{-3}	0.8814	3.21×10^{-2}	1.0320
Fe@NGHS	47.7	143	46.8	2.06×10^{-3}	0.7853	2.45×10^{-2}	1.1810
Co@NGHS	45.3	7.197	90.63	6.59×10^{-3}	1.1940	3.43×10^{-3}	0.6443
Fe&Co@NGHS	45.76	28.25	115.4	2.25×10^{-3}	0.9872	8.02×10^{-3}	0.5842
FeCo@GHS	33.52	4.41×10^{12}	235.7	1.66×10^{-3}	0.7897	2.58×10^{-2}	1.1850
NGHS	53.25	420.7	854.2	5.44×10^{-3}	0.7247	2.87×10^{-3}	0.9655
Pt/C	43.51	56.17	65.3	1.84×10^{-3}	0.7611	1.14×10^{-2}	0.9703

Note: R_s represents the solution resistance in the electrolyte, R_{int} represents the interface resistance of solid electrolyte, R_{ct} represents the charge transfer resistance, and CPE represents the constant phase element.

Table S6. Summary of the impedance fitting data for catalysts during OER process.

Catalyst	Impedance (Ω)		CPE(mF)	
	R_s	R_{ct}	CPE-T	CPE-P
FeCo@NGHS	50.52	36.18	1.61×10^{-3}	0.9212
Fe@NGHS	50.23	318.9	1.22×10^{-3}	0.8178
Co@NGHS	49.06	391.2	1.31×10^{-3}	0.7904
Fe&Co@NGHS	47.83	79.11	1.39×10^{-3}	0.8850
FeCo@GHS	47.99	277.7	1.42×10^{-3}	0.8467
NGHS	48.69	403.2	1.56×10^{-3}	0.8901
RuO_2	58.51	115.4	3.10×10^{-4}	0.9013

Table S7. Comparison of liquid and solid Zn-air performances of the FeCo@NGHS catalyst with recently reported advanced catalysts.

References	Catalysts	Liquid Zn-air battery		Solid Zn-air battery	
		Power density ($mW\ cm^{-2}$)	**Specific capacity ($mA\ h\ g^{-1}$)**	**Open-circuit voltage (V)**	**Power density ($mW\ cm^{-2}$)**
This work	FeCo@NGHS	121.19	802 (50 mA cm^{-2}) 800 (100 mA cm^{-2}) 786 (200 mA cm^{-2})	1.45	74.06
[25]	NPC/FeCo@NCNT	151.3	810 (200 mA cm^{-2})	1.45	65.0
[26]	Fe-Co_4N@NC	105	806 (5 mA cm^{-2})	1.34	72
[27]	IOSHs-NSC	133	768 (10 mA cm^{-2})	1.408	60
[28]	NGCNT/FeCo	89.3	653.2 (100 mA cm^{-2})	1.249	97.8
[29]	Co_3O_4/MnO_2/PQ	257	670 (10 mA cm^{-2})	1.2	45
[30]	Co-NDC	154	773 (5 mA cm^{-2})	1.4	45.9
[31]	Fe@Co-NMC	98.7	-	1.446	-
[32]	CoFe@NC	180	680 (10 mA cm^{-2})	1.35	-
[33]	CoP_x/Co-N_x-C@CNT	70	-	1.36	59
[34]	NCS@Co/CoO_x	182	816 (10 mA cm^{-2})	1.39	-
[35]	FeCo/N-CNTs@CC	132	-	1.4	127
[36]	CoN/FeN@N,SC-800	168.3	676 (2 mA cm^{-2})	1.353	-
[37]	CoP/FeP@PCN	175.4	780 (10 mA cm^{-2})	1.47	-
[38]	Co-MnO@NC/CC	172.5	711 (10 mA cm^{-2})	1.442	90

References

[1] X. Hao, Z. Jiang, X. Tian, X. Hao, Z.-J. Jiang, Facile assembly of Co-Ni layered double hydroxide nanoflakes on carbon nitride coated N-doped graphene hollow spheres with high electrochemical capacitive performance, Electrochim. Acta 253 (2017) 21-30.

[2] I.S. Amiinu, Z. Pu, X. Liu, K.A. Owusu, H.G.R. Monestel, F.O. Boakye, H. Zhang, S. Mu, Multifunctional Mo–N/C@MoS_2 Electrocatalysts for HER, OER, ORR, and Zn–Air Batteries, Adv. Funct. Mater. 27 (2017) 1702300.

[3] L. Liu, F. Yan, K. Li, C. Zhu, Y. Xie, X. Zhang, Y. Chen, Ultrasmall $FeNi_3N$ particles with an exposed active (110) surface anchored on nitrogen-doped graphene for multifunctional electrocatalysts, J. Mater. Chem. A 7 (2019) 1083-1091.

[4] G. Fu, Z. Cui, Y. Chen, Y. Li, Y. Tang, J.B. Goodenough, Ni_3Fe-N Doped Carbon Sheets as a Bifunctional Electrocatalyst for Air Cathodes, Adv. Energy Mater. 7 (2017) 1601172.

[5] Y. Fan, S. Ida, A. Staykov, T. Akbay, H. Hagiwara, J. Matsuda, K. Kaneko, T. Ishihara, Ni-Fe nitride nanoplates on nitrogen-doped graphene as a synergistic catalyst for reversible oxygen evolution reaction and rechargeable Zn-air battery, Small 13 (2017) 1700099.

[6] G. Fu, Z. Cui, Y. Chen, L. Xu, Y. Tang, J.B. Goodenough, Hierarchically mesoporous nickel-iron nitride as a cost-efficient and highly durable electrocatalyst for Zn-air battery, Nano Energy 39 (2017) 77-85.

[7] L. Yang, X. Zeng, D. Wang, D. Cao, Biomass-derived FeNi alloy and nitrogen-codoped porous carbons as highly efficient oxygen reduction and evolution bifunctional electrocatalysts for rechargeable Zn-air battery, Energy Storage Mater. 12 (2018) 277-283.

[8] Y. Wang, G. Zhang, M. Ma, Y. Ma, J. Huang, C. Chen, Y. Zhang, X. Sun, Z. Yan, Ultrasmall NiFe layered double hydroxide strongly coupled on atomically dispersed FeCo-NC nanoflowers as efficient bifunctional catalyst for rechargeable Zn-air battery, Sci. China Mater. 63 (2020) 1182-1195.

[9] W. Yan, Z. Yang, W. Bian, R. Yang, $FeCo_2O_4$/hollow graphene spheres hybrid with

enhanced electrocatalytic activities for oxygen reduction and oxygen evolution reaction, Carbon 92 (2015) 74-83.

[10] X. Zhang, H. Xu, X. Li, Y. Li, T. Yang, Y. Liang, Facile Synthesis of Nickel–Iron/Nanocarbon Hybrids as Advanced Electrocatalysts for Efficient Water Splitting, ACS Catal. 6 (2016) 580-588.

[11] T. An, X. Ge, N.N. Tham, A. Sumboja, Z. Liu, Y. Zong, Facile One-Pot Synthesis of CoFe Alloy Nanoparticles Decorated N-Doped Carbon for High-Performance Rechargeable Zinc–Air Battery Stacks, ACS Sustain. Chem. Eng. 6 (2018) 7743-7751.

[12] P. Cai, Y. Hong, S. Ci, Z. Wen, In situ integration of CoFe alloy nanoparticles with nitrogen-doped carbon nanotubes as advanced bifunctional cathode catalysts for Zn–air batteries, Nanoscale 8 (2016) 20048-20055.

[13] G. Fu, Y. Chen, Z. Cui, Y. Li, W. Zhou, S. Xin, Y. Tang, J.B. Goodenough, Novel Hydrogel-Derived Bifunctional Oxygen Electrocatalyst for Rechargeable Air Cathodes, Nano Lett. 16 (2016) 6516-6522.

[14] M. Prabu, K. Ketpang, S. Shanmugam, Hierarchical nanostructured $NiCo_2O_4$ as an efficient bifunctional non-precious metal catalyst for rechargeable zinc–air batteries, Nanoscale 6 (2014) 3173-3181.

[15] S. Gupta, S. Zhao, X.X. Wang, S. Hwang, S. Karakalos, S.V. Devaguptapu, S. Mukherjee, D. Su, H. Xu, G. Wu, Quaternary FeCoNiMn-Based Nanocarbon Electrocatalysts for Bifunctional Oxygen Reduction and Evolution: Promotional Role of Mn Doping in Stabilizing Carbon, ACS Catal. 7 (2017) 8386-8393.

[16] Y. Tian, L. Xu, J. Bao, J. Qian, H. Su, H. Li, H. Gu, C. Yan, H. Li, Hollow cobalt oxide nanoparticles embedded in nitrogen-doped carbon nanosheets as an efficient bifunctional catalyst for Zn–air battery, J. Energy Chem. 33 (2019) 59-66.

[17] B. Fang, J. Yang, C. Chen, C. Zhang, D. Chang, H. Xu, C. Gao, Carbon Nanotubes Loaded on Graphene Microfolds as Efficient Bifunctional Electrocatalysts for the Oxygen Reduction and Oxygen Evolution Reactions, ChemCatChem 9 (2017) 4520-4528.

[18] M. Zhu, J. Nong, P. Xie, A.S. Zhu, M.Z. Rong, M.Q. Zhang, Well-dispersed CoO embedded in 3D N-S-doped carbon framework through morphology-retaining pyrolysis as efficient oxygen reduction and evolution electrocatalyst, Electrochim. Acta 295 (2019) 624-631.

[19] S.J. Ha, J. Hwang, M.J. Kwak, J.C. Yoon, J.H. Jang, Graphene-Encapsulated Bifunctional Catalysts with High Activity and Durability for Zn-Air Battery, Small 19 (2023) e2300551.

[20] P. Zhang, S. Liu, J. Zhou, L. Zhou, B. Li, S. Li, X. Wu, Y. Chen, X. Li, X. Sheng, Y. Liu, J. Jiang, Co-Adjusting d-Band Center of Fe to Accelerate Proton Coupling for Efficient Oxygen Electrocatalysis, Small 20 (2024) e2307662.

[21] L. Peng, X. Peng, Z. Zhu, Q. Xu, K. Luo, Z. Ni, D. Yuan, Efficient MnO and Co nanoparticles coated with N-doped carbon as a bifunctional electrocatalyst for rechargeable Zn-air batteries, Int. J. Hydrogen Energy 48 (2023) 19126-19136.

[22] J.H. Kim, M. Kim, J.H. Hong, J.-K. Lee, Y.C. Kang, Novel design and synthesis of multi-anionic Co(OH)Se with ZIF-67 derived porous carbon matrix as a bifunctional electrocatalyst for rechargeable Zn-air batteries, Chem. Eng. J. 467 (2023) 143359.

[23] L. Bo, W. Shi, F. Nian, Y. Hu, L. Pu, P. Li, Z. Zhang, J. Tong, Interface engineering of Co_3S_4@Co_3O_4/N, S-doped carbon core@shell nanostructures serve as an excellent bifunctional ORR/OER electrocatalyst for rechargeable Zn-air battery, Sep. Purif. Technol. 307 (2023) 122536.

[24] Y. Qian, Z. Hu, X. Ge, S. Yang, Y. Peng, Z. Kang, Z. Liu, J.Y. Lee, D. Zhao, A metal-free ORR/OER bifunctional electrocatalyst derived from metal-organic frameworks for rechargeable Zn-Air batteries, Carbon 111 (2017) 641-650.

[25] X. Hao, Z. Jiang, B. Zhang, X. Tian, C. Song, L. Wang, T. Maiyalagan, X. Hao, Z.J. Jiang, N-Doped Carbon Nanotubes Derived from Graphene Oxide with Embedment of FeCo Nanoparticles as Bifunctional Air Electrode for Rechargeable Liquid and Flexible All-Solid-State Zinc-Air Batteries, Adv. Sci. 8 (2021) 2004572.

[26] Q. Xu, H. Jiang, Y. Li, D. Liang, Y. Hu, C. Li, In-situ enriching active sites on co-doped Fe-Co_4N@N-C nanosheet array as air cathode for flexible rechargeable Zn-air batteries, Appl. Catal. B-Environ. 256 (2019) 117893.

[27] K. Tang, C. Yuan, Y. Xiong, H. Hu, M. Wu, Inverse-opal-structured hybrids of N, S-codoped-carbon-confined Co_9S_8 nanoparticles as bifunctional oxygen electrocatalyst for on-chip all-solid-state rechargeable Zn-air batteries, Appl. Catal. B-Environ. 260 (2020) 118209.

[28] C.-Y. Su, H. Cheng, W. Li, Z.-Q. Liu, N. Li, Z. Hou, F.-Q. Bai, H.-X. Zhang, T.-Y. Ma, Atomic Modulation of FeCo-Nitrogen-Carbon Bifunctional Oxygen Electrodes for Rechargeable and Flexible All-Solid-State Zinc-Air Battery, Adv. Energy Mater. 7 (2017) 1602420.

[29] X. Li, F. Dong, N. Xu, T. Zhang, K. Li, J. Qiao, Co_3O_4/MnO_2/Hierarchically Porous Carbon as Superior Bifunctional Electrodes for Liquid and All-Solid-State Rechargeable Zinc-Air Batteries, ACS Appl. Mater. Interfaces 10 (2018) 15591-15601.

[30] Z. Chen, Q. Wang, X. Zhang, Y. Lei, W. Hu, Y. Luo, Y. Wang, N-doped defective carbon with trace Co for efficient rechargeable liquid electrolyte-/all-solid-state Zn-air batteries, Sci. Bull. 63 (2018) 548-555.

[31] Y. Zhang, Y. li, K. Shi, Z. Zhu, X. Li, H. Xu, J. Gao, Bimetallic dispersion zeolitic imidazolate framework derived spherical porous bifunctional catalysts for liquid/solid Zn-Air batteries, J. Alloy Compd. 925 (2022) 166680.

[32] S. Ren, P. Zhang, X. Tang, H. Zheng, Z. Wan, Porous nitrogen-doped carbon nanocages decorated with bimetallic iron/cobalt sites as superior oxygen catalysts for liquid and all-solid-state Zn–air batteries, J. Energy Storage 83 (2024).

[33] X. Wu, S. Chen, Y. Feng, Q. Yuan, J. Gao, Y. Chen, Y. Huang, Y.B. He, W. Gan, Microwave-assisted synthesis of carbon nanotubes threaded core-shell CoP /Co-N -C@CNT and its performance as an efficient bifunctional oxygen catalyst for the rechargeable zinc-air battery, Mater. Today Phys. 9 (2019) 100132.

[34] L. Zhong, H. Zhou, R. Li, H. Cheng, S. Wang, B. Chen, Y. Zhuang, J. Chen, A.

Yuan, Co/CoO_x heterojunctions encapsulated N-doped carbon sheets via a dual-template-guided strategy as efficient electrocatalysts for rechargeable Zn-air battery, J. Colloid Interface Sci. 599 (2021) 46-57.

[35] Z. Li, H. Yang, H. Sun, S. Liang, G. Lu, Z. Liu, S. Kou, Highly Nitrogen-Doped Carbon Nanotube Nanoarrays as Self-supported Bifunctional Electrocatalysts for Rechargeable and Flexible Zinc-Air Batteries, ACS Sustain. Chem. Eng. 9 (2021) 4498-4508.

[36] S. Ren, X. Duan, M. Lei, S. Liang, M. Zhang, H. Zheng, Energetic MOF-derived cobalt/iron nitrides embedded into N, S-codoped carbon nanotubes as superior bifunctional oxygen catalysts for Zn–air batteries, Appl. Surf. Sci. 569 (2021) 151030.

[37] K. Chen, L. Wang, J. Long, F. Zhao, L. Kang, Petaloid CoP/FeP Composites: Efficiently bifunctional cathode electrochemical oxygen catalysts for aqueous and Solid-State Zinc-Air batteries, Chem. Eng. J. 496 (2024) 153820.

[38] Q. Liu, P. Qiao, M. Tong, Y. Xie, X. Zhang, K. Lin, Z. Liang, L. Wang, H. Fu, Enhancing zinc–air battery performance by constructing three-dimensional N-doped carbon coating multiple valence Co and MnO heterostructures, Nano Res. 17 (2024) 5104-5113.